

This article appeared in a journal published by Elsevier. The attached copy is furnished to the author for internal non-commercial research and education use, including for instruction at the authors institution and sharing with colleagues.

Other uses, including reproduction and distribution, or selling or licensing copies, or posting to personal, institutional or third party websites are prohibited.

In most cases authors are permitted to post their version of the article (e.g. in Word or Tex form) to their personal website or institutional repository. Authors requiring further information regarding Elsevier's archiving and manuscript policies are encouraged to visit:

<http://www.elsevier.com/copyright>



Signal transport in Computed Tomography detectors

B.J. Heismann^{a,c,*}, L. Bätz^a, K. Pham-Gia^b, W. Metzger^b, D. Niederlöhner^a, S. Wirth^a

^aSiemens Medical Solutions, Erlangen, Germany

^bSiemens Corporate Technology, Munich, Germany

^cUniversity of Erlangen, Institute of Pattern Recognition, Erlangen, Germany

Available online 20 March 2008

Abstract

In Computed Tomography (CT) X-ray intensities are measured by large-scale solid-state detectors. The standard set-up comprises a scintillator pixel array attached to a matrix of photo sensors, which in turn is read out by analog-to-digital conversion electronics. We have developed and validated a three-dimensional system model describing the cascaded system process. The first step comprises a Monte-Carlo (MC) tracking of the primary X-ray quanta energy deposition, taking into account the relevant fluorescence and scattering processes. The second step models the transport of optical photons in the scintillator pixels formed by a solid-state bulk with surrounding back-scattering TiO₂ walls. In a third step the individual events are integrated to a read-out signal and analyzed for their statistical properties. The system model is verified by a comparison to optical measurements. A scintillator array is excited by a needle beam X-ray source. The emitted light field is read out by a high-resolution CCD sensor. A good agreement between simulation and experiments is found, with a typical deviation in the range of 5%. The detector response function $D(E, E')$ is used to quantify the spectral behavior. It yields the probability to measure an energy E' for an incoming quantum energy E . We calculate the expected energy $\langle E'(E) \rangle$ and link the deviations from proportionality in E to properties of the signal transport. Finally the impact of the signal transport statistics on the output signal-to-noise ratio is analyzed.

© 2008 Elsevier B.V. All rights reserved.

PACS: 87.57.Q-; 87.57.cm; 87.59.-e

Keywords: Scintillator detector; Computed tomography; Detector response function; Modulation transfer function

1. Introduction

Scintillator detectors are state-of-the-art in Computed Tomography (CT) X-ray detection. Especially GdOS-based materials combine high stopping power and light yield with low signal lag, i.e. afterglow. They are commonly embedded into highly back-scattering TiO₂ epoxy compounds to build up pixel arrays with pitches in the range of 0.5 to several mm.

Fig. 1 shows the basic processes during detection. Incoming X-ray quanta deposit energy in the bulk, generating secondary light photons. Optical transport of the photons takes place. A photo sensor element at the

bottom surface of the pixel volume collects incoming photons. Its current is integrated and converted to digital information by an analog-to-digital converter.

In this paper we present a detailed physical modeling of the cascaded detection process [1]. On a microscopic level we establish a Monte-Carlo (MC) simulation for tracking individual X-ray quanta and their conversion to digital output information. The X-ray absorption, scattering and fluorescence as well as light generation, transfer and detection processes are modeled. We verify the simulation by comparing CCD-based scintillator array light output and cross-talk measurements to simulated data.

On the macroscopic scale the behavior of an irradiated pixel is described by the probability density $D(E, E')$ to measure an energy E' at an input energy E . We use it to describe the impact of signal transport properties on the spectral linearity and signal-to-noise-ratio (SNR) of the output signals.

*Corresponding author at: Siemens AG, Computed Tomography Division, Forchheim, Germany. Tel.: +49 9191 188707; fax: +49 9191 188731.

E-mail address: bjoern.heismann@siemens.com (B.J. Heismann).

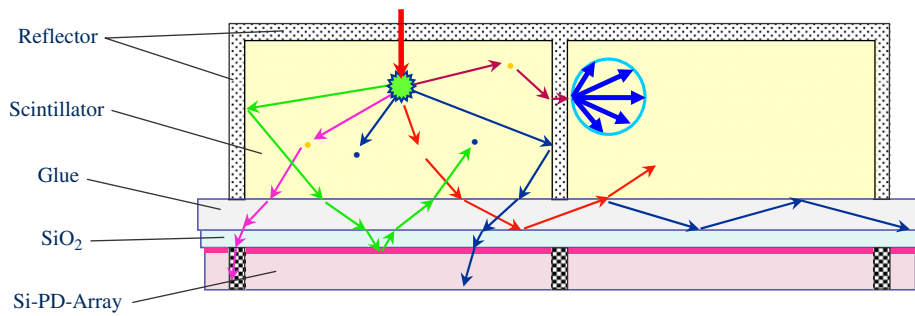


Fig. 1. Examples of signal transport processes in a scintillator detector. A primary X-ray quantum is absorbed. Generated light quanta are scattered and absorbed in the bulk, interact with the back-scattering TiO₂ septa and get detected in the pixelated Si photodiode array.

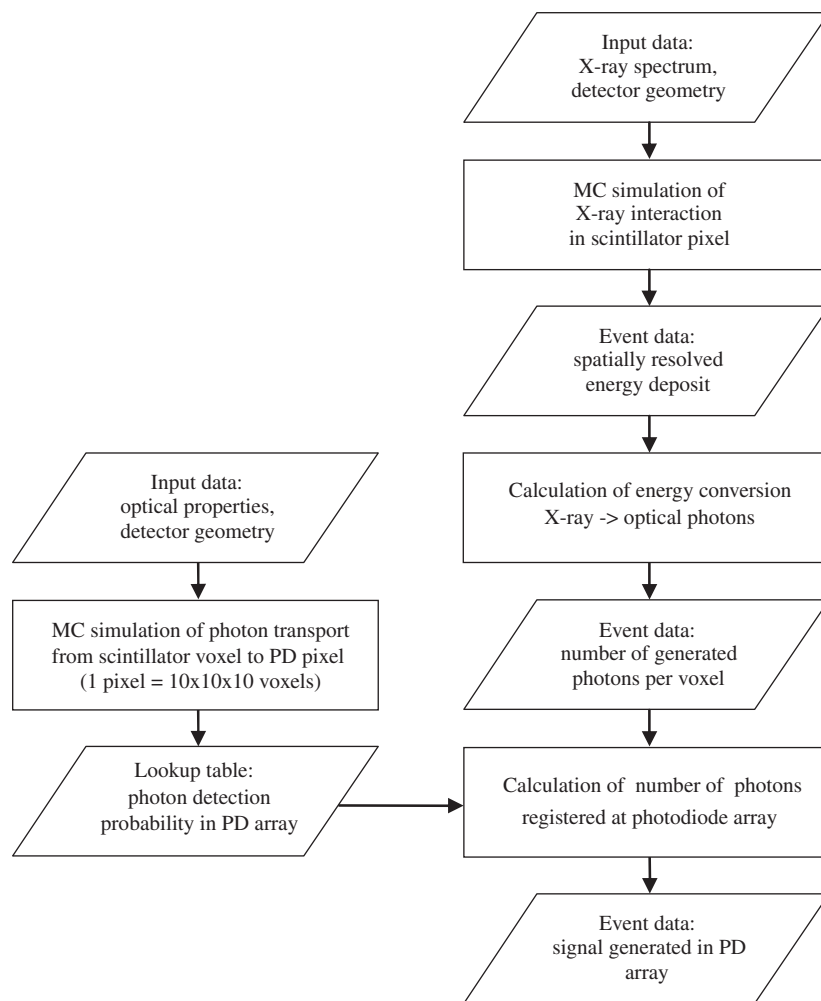


Fig. 2. Physical model of signal transport in a scintillator detector. The right branch calculates the X-ray energy deposition, the left branch the light photon detection probabilities. By multiplying and summing the photo sensor signal is generated, see Fig. 3.

2. Physical modeling

The signal transport model of X-ray detection in the scintillator detector is shown in Fig. 2. The physical processes are split up into (a) the X-ray energy deposition and (b) the optical transport.

2.1. X-ray energy deposition

The X-ray spectrum and field distribution, as well as the scintillator geometry are input parameters to the first step. A MC simulation of X-ray interaction physics [2–4] is used to calculate the X-ray energy deposition. It includes all

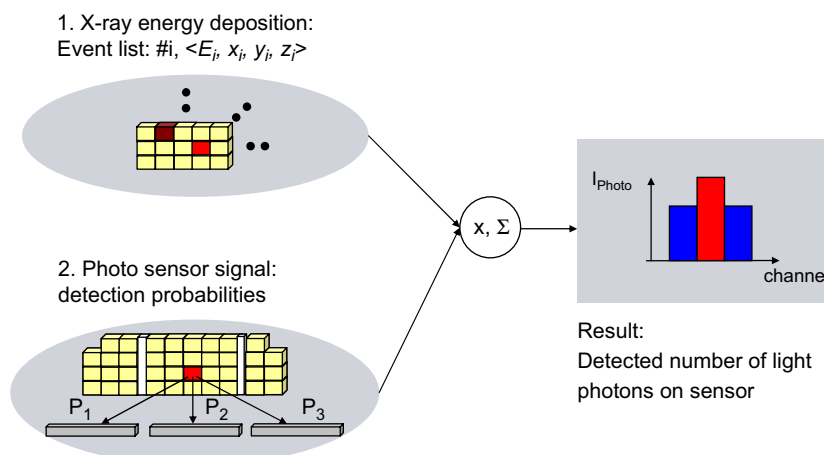


Fig. 3. Calculation scheme for the photosensor signal.

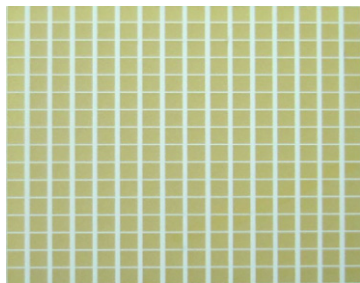


Fig. 4. Reference scintillator geometry used in the measurements and simulations of Fig. 5a, b. The pitch along the vertical (y) and horizontal (x) axis is $p_y = \sim 1.2$ mm and $p_x = \sim 1.0$ mm. The TiO_2 septa have a width of $d_y = 80$ μm and $d_x = 250$ μm .

relevant physical processes including tracking of fluorescence and Compton events. We obtain a list of events indexed by n , each comprising a number $i(n) \geq 1$ of energy deposition values ΔE_i at interaction sites $r_i = (x_i, y_i, z_i)$.

2.2. Light transport

The scintillator geometry and measured optical parameters like the scattering and transmission coefficients of the materials are input to the second step. For an absorbed quantum of energy E , the equivalent energy gE is generated in photons. For GdOS:Pr, we have $g = 12 \pm 2\%$, i.e. around 60 photons/keV are emitted isotropically. Light propagation, scattering, absorption and reflection in the geometry of Fig. 1 is calculated for individual light photons [5]. The probability to detect a light photon in the photosensor for a given starting position $r = (x, y, z)$ is calculated in the second step.

In order to generate the signal readout of the photosensor in Fig. 1, we multiply the energy deposition information of step 1 with the local detection probability of step 2. Fig. 3 illustrates this process.

3. Comparison to measurement

In order to validate our model we have measured the light output of various scintillator configurations and

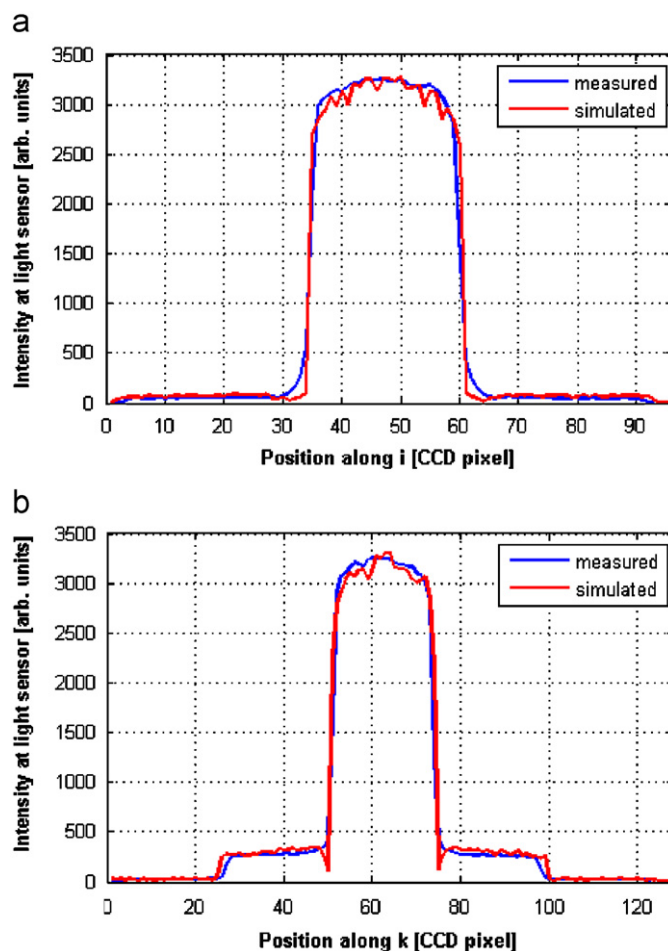


Fig. 5. (a,b) Measured and simulated light-output of a scintillator array irradiated with a needle beam directed at the center of the pixel.

compared the results to simulations. The following settings are used: A needle X-ray beam composed of a 120 kV tube spectrum is directed at the center of a scintillator pixel shown in Fig. 4. A fiber coupling picks up the light emitted from the bottom surface of the scintillator and couples it into a CCD sensor with 43 μm pixel pitch. Fig. 5a and b

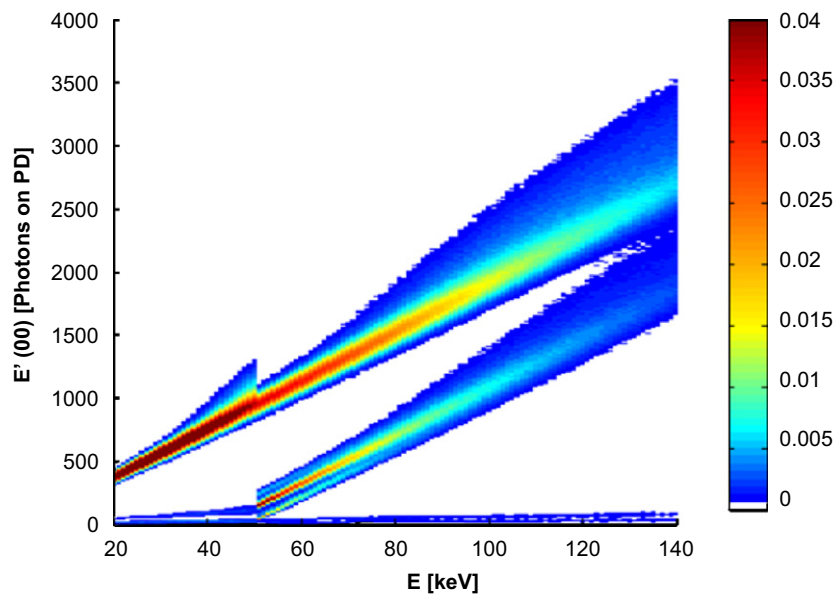


Fig. 6. Detector response function $D(E, E')$, calculated for flat-field irradiation of a scintillator pixel.

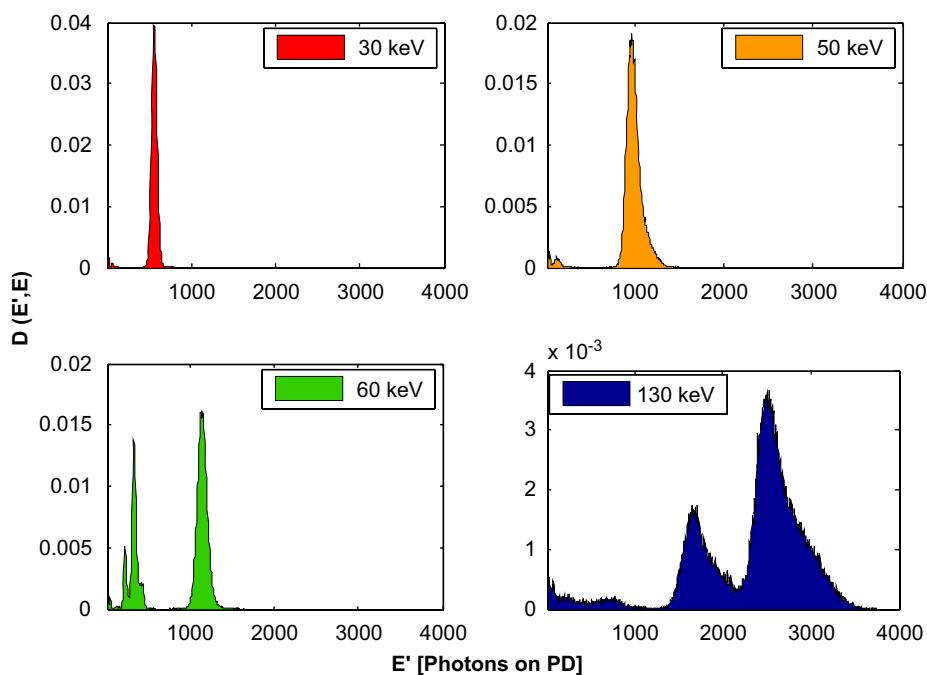


Fig. 7. Detector response for various constant input energies.

shows the measured and simulated light output profiles along the horizontal and vertical axis of the scintillator array of Fig. 4.

Both simulation and measurement show the substantial cross-talk between pixels of the scintillator. Cross-talk in the vertical direction, Fig. 5b, is higher due to the smaller septa in that direction.

When comparing measurement and simulation the cross-talk profiles and averaged pixel values are reproduced with a precision in the range of 5%. The main deviations occur at the edges where the measurements appear more

smoothed. This is explained by the limited point-spread function of the fiber coupling plate. From its fiber core diameter of around $50\ \mu\text{m}$, we can expect a convolution of the scintillator output with a sinc function of $f_0 = 10\ \text{mm}^{-1}$. This corresponds well to the observed low-pass filtering of the measured data.

4. Results

We use the detector response function $D(E, E')$ as our macroscopic figure of merit to quantify the spectral

behavior of the scintillator detector. For an incoming quantum of energy E it yields the probability distribution to measure an effective output energy E' . A monoenergetic flat-field irradiation of the central pixel is used in the physical modeling.

Fig. 6 depicts the resulting $D(E, E')$. For input energies $E < 50.2$ keV the output energies E' are mostly linear in E . However, light tailing occurs increasingly. This is due to the fact that quanta are absorbed closer to the photo sensor with increasing X-ray energies. The light has to travel shorter distances, leading to a larger equivalent energy signal on the photosensor. For $E > 50.2$ keV fluorescence at the Gd K-edge takes place. A second branch with lower output energies occurs. A fine structure of the K_α and K_β escape energy differences is visible. With increasing input energy light tailing gets stronger and primary quantum absorption decreases. Fig. 7 shows this for the constant energies $E = 30, 50, 60$ and 130 keV. Note that the secondary peak has almost the same height and weight as the primary peak for $E = 60$ keV.

The secondary peak height decreases with increasing energy E . This is due to two facts: First, the primary quantum absorption has the well-known exponential behavior. The average interaction depth increases with E and is always situated in the upper half of the pixel. Second, the re-absorption probability of the fluorescence quantum within the pixel has its maximum when emitted at the center of the pixel. It decreases when approaching the top and bottom surfaces. Thus the re-absorption probability increases with energy E and the event is more likely registered in the main peak. This explains the observed peak height ratio as a function of energy.

Compton scatter energy deposition events are visible for $E = 130$ keV at small output energies. In these events the

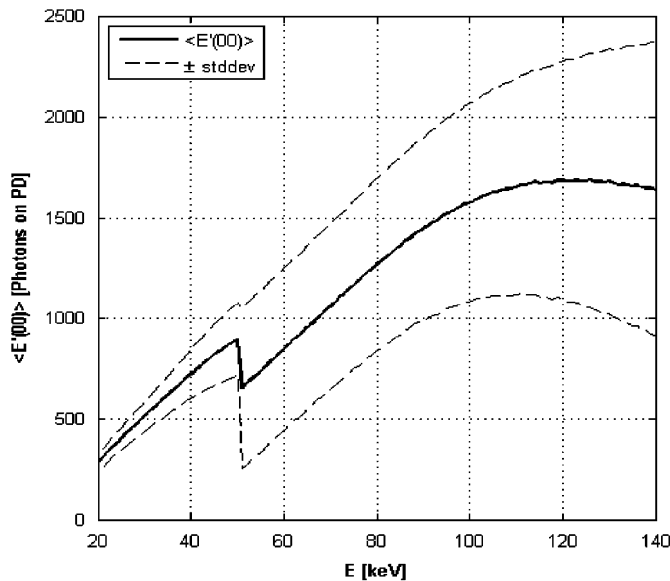


Fig. 8. Expected energy output $\langle E'(E) \rangle$ and its standard deviation for the scintillator pixel as a function of energy.

corresponding Compton scattered photon left the pixel volume.

The average detected energy $\langle E'(E) \rangle$ calculated from $D(E, E')$ is shown in Fig. 8. The deviation from proportionality to E is substantial. The causes derived from Fig. 6 in order of importance are (a) fluorescence escapes, (b) light tailing, (c) reduced X-ray quantum absorption with increasing energies and (d) Compton scattering.

The dashed line in Fig. 8 shows the variance of the output signal. It increases significantly beyond the K-edge. We can calculate the impact on the SNR with statistics developed in the framework of cascaded gain blurring processes [1,6].

Our measured light signal Y is the sum over the energies E'_i generated by N quanta:

$$Y = \sum_{i=1}^N E'_i \quad (1)$$

Note that both N and E'_i are random variables. The statistics of Y are given by

$$\langle Y \rangle = \langle E' \rangle \langle N \rangle \quad (2a)$$

$$\sigma(Y) = \sqrt{\langle N \rangle} \sqrt{\left(\langle E' \rangle^2 + \sigma^2(E') \right)}. \quad (2b)$$

This yields the generalized Swank factor [7]

$$A_s(E) = \frac{1}{\alpha(E)} \left(\frac{\text{SNR}_{\text{out}}}{\text{SNR}_{\text{in}}} \right)^2 = \frac{\langle E' \rangle^2}{\langle E' \rangle^2 + \sigma^2(E')}, \quad (3)$$

describing the Poisson excess noise caused by the signal transport processes. By inserting the data of Fig. 8 into Eq. (3), we obtain Fig. 9. We have $A_s(E) = \sim 0.97$ for $E < E_{\text{K-edge}} = 50.2$ keV, a drop to around 0.75 at $E_{\text{K-edge}}$, a subsequent increase to around $A_s(E) = 0.91$ at $E = 100$ keV and a drop to $A_s(E) = 0.84$ for $E = \sim 140$ keV. Note that fluorescence escape and optical transport dominate $\sigma^2(E')$ and $A_s(E)$, whereas the primary gain

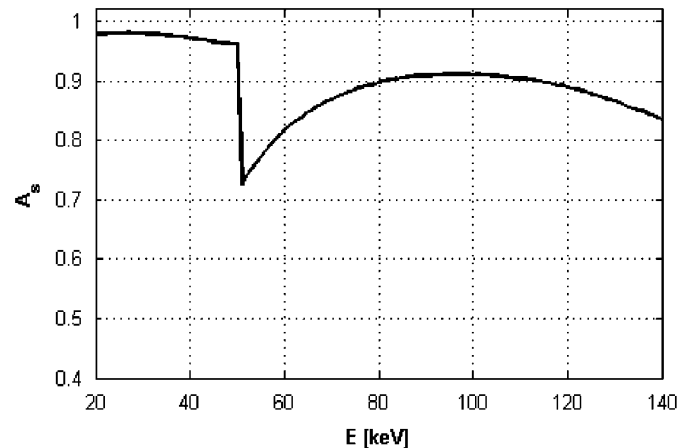


Fig. 9. Influence of scintillator signal transport on output SNR as described by Eq. (3).

blurring of the X-ray energy deposition plays only a minor role.

5. Conclusion

We have established a cascaded full-3D physical modeling of X-ray deposition and optical signal transport in scintillator arrays. The simulations are compared to CCD-based light output measurements and agree typically within 5%. The probability density $D(E, E')$ to measure E' for an incoming energy E is used to describe the macroscopic behavior. We find that the expected mean energy $\langle E'(E) \rangle$ has significant deviations from a proportionality to E . The main contribution to this effect is the fluorescence escape of quanta beyond the scintillator K-edge. Light transport tailing, reduced scintillator bulk absorption with increasing energy and Compton scatter events are further sources. Finally, the SNR loss of the output signal due to transport processes has been evaluated. A drop of around 25% is found at the K-edge. Fluorescence escape is the dominating gain blurring process in pixelated CT scintillator detectors.

References

- [1] I.A. Cunningham, Applied linear system theory, in: J. Beutel, H.L. Kundel, R.L. van Metter (Eds.), Handbook of Medical Imaging, vol. 1, SPIE, 2000, p. 79.
- [2] K. Stierstorfer, Mocassim Monte-Carlo simulation tool, using sources [3–4], personal communication (2007).
- [3] Tables and Graphs of Atomic Subshell and Relaxation Data Derived from the LLNL Evaluated Atomic Data Library (EADL), $Z = 1-100$, S.T.Perkins, D.E.Cullen, M.H.Chen, J.H.Hubbell, J.Rathkopf, J.Scofield, UCRL-50400, vol.30, 1991.
- [4] Tables and Graphs of Photon-Interaction Cross Sections from 10 eV to 100 GeV, LLNL Evaluated Photon Data Library (EPDL), UCRL-50400, Vol. 6, Rev. 4, D.E. Cullen, M H Chen, J H Hubbell, S.T. Perkins, E F Plechaty, J A Rathkopf, J H Scofield, Lawrence Livermore National Laboratory, 1989.
- [5] S. Wirth, K. Pham-Gia, W.Metzger, B.J. Heismann, M11-212, in: IEEE Medical Imaging Conference Record, 2006.
- [6] M. Rabbani, R. Shaw, R. Van Metter, Detective quantum efficiency of imaging systems with amplifying and scattering mechanisms, J. Opt. Soc. Am. A 4 (1987) 895–901.
- [7] R.W. Swank, Absorption and noise in X-ray phosphors, J. Appl. Phys. 44 (1973) 4199–4203.